

Theoretical Investigation and Reconsideration of Intramolecular Proton-Transfer-Induced the Twisted Charge-Transfer for the Fluorescent Sensor to Detect the Aluminum Ion

Xiumin Liu

Dalian Polytechnic University

Hengwei Zhang

Dalian Polytechnic University

Sen Liu

Dalian Polytechnic University

Yi Wang (✉ wangyi@dlpu.edu.cn)

Dalian Polytechnic University

Peng Zhang

Dalian Polytechnic University

Research Article

Keywords: Aluminum sensor, Excited state intramolecular proton transfer, Fluorometric sensor, OFF-ON type, Twisted charge transfer

Posted Date: March 28th, 2022

DOI: <https://doi.org/10.21203/rs.3.rs-1460369/v1>

License:  This work is licensed under a Creative Commons Attribution 4.0 International License.

[Read Full License](#)

Version of Record: A version of this preprint was published at Structural Chemistry on April 25th, 2022. See the published version at <https://doi.org/10.1007/s11224-022-01941-z>.

Abstract

A Schiff base compound 6-amino-5-(((2-hydroxynaphthalen-1-yl)methylene)amino)-2-mercaptopyrimidin-4-ol (AHM) in acetonitrile solvent is found to show "OFF-ON type" mode upon addition of Al^{3+} ion and successfully applied for selective recognition of Al^{3+} ion. In this work, the reconsideration of excited state intramolecular proton transfer (ESIPT) and twisted intramolecular charge transfer (TICT) have been explored in detail based on density functional theory (DFT) and time-dependent density functional theory (TD-DFT) methods. In the absence of Al^{3+} , the lone pair electrons are transferred from $-\text{C}=\text{N}$ to $-\text{OH}$ forming a hydrogen-bonding configuration, and AHM shows weak fluorescence. When AHM is coordinate with metal ion, the TICT state is eliminated, and emission is significantly enhanced. Thus, in this paper, the origination of the non-emissive behavior of AHM has been explained in detail. The frontier molecular orbitals (MOs) and hole-electrons are used to analyze the charge distribution, providing strong evidence for the possibility of ESIPT and TICT processes occurring.

Introduction

Metal ions are closely related to the basic processes of living systems and human health problems [1–3]. Aluminum is the most abundant metal in the crust, and its elemental elements and compounds are widely used in production and life [4]. In recent years, the utilization of aluminum has been increased to food additives [5, 6], construction [7], medicine, ceramics, cosmetics and other fields. However, with the widespread use of aluminum and its alloys, the content of aluminum in soil and water gradually increased, resulting in the accumulation of Al^{3+} in food, water, air, etc. In addition, prolonged exposure to high levels of Al^{3+} is toxic to the kidney, liver, brain and nervous system [8–11]. Moreover, the abnormal concentration of Al^{3+} has adverse effects on the growth of seeds and root systems [12, 13]. Thus, timely monitoring of Al^{3+} levels in humans and the natural environment is needed to prevent the direct effects of Al^{3+} on the biosphere and human health [14]. In the previous report, the detection techniques have been defected because of the lack of coordination and spectrum performance. In recent years, chemical sensors used for monitoring biological and environment-related metal ions have been studied by researchers because of their advantages of simple synthesis route and high selectivity [15–19].

It is found that the closing sensor usually produces low signal output during binding, which can easily interfere with the time separation of similar compounds by time-resolved fluorescence method [20, 21]. Thus, many studies are inclined to the design and application of opening the sensor. Moreover, Al^{3+} is a fluorescence quencher due to its paramagnetism, which could affect the information of 'turn-on' fluorescent sensors for its detection [22–24]. In addition, selective binding of organic functional groups is one of the rational strategies for designing excellent fluorescent probes. Schiff base derivatives contain strong donor position (imine nitrogen atoms) which could provide a nitrogen-rich oxygen coordination environment [25, 26]. Moreover, Quinoline is also an ideal tool for metal ion fluorescence sensing based on good water solubility, good biocompatibility and large Stokes shift [27–29]. Generally, the practical

chemical sensors mainly rely on various types of fluorescence mechanisms, such as ESIPT [30], photoinduced electron transfer (PET) and ICT mechanisms [31–33].

AHM is a sensor to show turn-on type, which is synthesized by Yadav *et al* [34]. The sensor AHM is consist of two parts, named A part and B part, which are connected by a carbon-nitrogen double bond (C = N), as shown in Scheme 1. Moreover, the imine nitrogen atom is able to transfer an electron to the hydroxyl-naphthalene, and the proton on the hydroxyl-naphthalene unit is transferred to the imine nitrogen, resulting in intramolecular hydrogen bond. Schiff bases bearing a C = N structure could easily isomerize and tend to exhibit very weak fluorescence. However, the Schiff base, with π electrons in C $\frac{1}{2}$ N group offers a good possibility for chelation with metal ions. Thus, when AHM and Al³⁺ form the complex, the C = N isomerization is inhibited and the fluorescence performance is enhanced. First, the presence of C = N double bonds may lead to a TICT. It is worth noting that there are two hydroxyl groups in AHM molecule, whether both can induce ESIPT reaction remains to be discussed, which are not considered in the experiment. Meanwhile, the photophysical characteristics of sensor AHM are complicated and the detection mechanism of sensor AHM and Al³⁺ is also lack of theoretical research. Here, the photophysical properties and sensing mechanism of AHM will be investigated. The charge transfer process is studied by hole-electron analysis and the variation of various parameters. In addition, the possible non-emission channels are studied by relaxation scanning. The detection mechanism of the sensor is analyzed in detail by studying the three-coordination structure between Al³⁺ and the sensor.

Computation details

1. All calculations were accomplished with the Gaussian16 program package [35] by using DFT and TDDFT methods. B3LYP functional [36] and TZVP basis set [37, 38] were selected to serve the calculation. The B3LYP functional is of 20% Hartree-Fock exchange, and has a low requirement for lattice point integration. In addition, the polarizable continuum model using the integral equation formalism variant (IEFPCM) was applied with acetonitrile (ACN) as the solvent simulating the experiment environment [39].

2. We optimize the structures of AHM-a, AHM-b and AHM-c in the S₀ and S₁ states without setting any restrictions on symmetry, bonds, angles, and calculate the IR frequencies in the same calculation level. It is proved that the molecular structures of our optimized AHM-c are at the local lowest point. The only imaginary frequency along with hydrogen bond orientation represents the transition-state structure of ESIPT reaction.

3. The calculated electron spectra are comparable with the experimental value, which show the reliability of the selected theoretical calculation method. Moreover, the charge transfer process is studied by hole-electron analysis. The degree of charge transfer is measured using the value of the centroid distance (D) index, the degree of overlap (S_r), the width distribution (H), degree of separation (t), hole delocalization index (HDI) and electron delocalization index (EDI), which are introduced by using the Multiwfn program [40, 41]. All the formulas are as follows:

$$D_x = |X_{ele} - X_{hole}| \quad D_y = |Y_{ele} - Y_{hole}| \quad D_z = |Z_{ele} - Z_{hole}|$$

$$D \text{ index} = \sqrt{(D_x)^2 + (D_y)^2 + (D_z)^2}$$

$$S_r \text{ index} = \int S_r(r) dr \equiv \int \sqrt{\rho^{hole}(r) \rho^{ele}(r)} dr$$

$$H \text{ index} = (|\sigma_{ele}| + |\sigma_{hole}|) / 2$$

$$t \text{ index} = D \text{ index} \cdot |H \cdot u_{CT}|$$

$$HDI = 100 \times \sqrt{\int [\rho^{hole}(r)]^2 dr}$$

$$EDI = 100 \times \sqrt{\int [\rho^{ele}(r)]^2 dr}$$

4. We have used Multiwfn software to study the type of hydrogen bond interaction by applying RDG function. The formula is as follows:

$$RDG(r) = \frac{1}{2} \frac{|\Delta\rho(r)|}{(3\pi^2)^{1/3} \rho(r)^{4/3}}$$

The weak interactions depend on the λ_2 of eigenvalue and the ρ of electron density in view of Bader's atoms-in-molecules (AIM) theory. The relationship between them is as follows:

$$\Omega(r) = \text{Sign}(\lambda_2(r)) \rho(r)$$

Results And Discussion

Geometrical information of fluorescent sensor AHM

The sensor AHM has been optimized in the S_0 state. The optimized geometric structures are shown in Fig. 1b (referred to AHM-a). In Table 1, the $\angle C_3C_2N_1C_4$ is 157° , meanwhile, two single bonds, named C_2-N_1 and C_4-C_5 are observed, and the rotation between the single bonds makes the structure of AHM more flexible. Additionally, the distance between H_2-N_1 is 3.66 \AA , and there is no intramolecular hydrogen bond between them. However, there is a hydrogen bond between H_1 and N_1 with a bond length of 1.64 \AA and the $O_1H_1N_1$ angle of 149° , which prevents the rotation of the intramolecular single bond. Thus, it is not necessary to consider the rotation forces caused by the C_4-C_5 deformation. To investigate the rotation of

the C₂-N₁ single bond, relaxation scanning of the C₃C₂N₁C₄ dihedral is performed. We have obtained a rotamer with a C₃C₂N₁C₄ dihedral angle of 47°, abbreviated as AHM-b (Fig. 1a). Furthermore, Fig. 1d shows that in the S₀ state, the relative energy of AHM-a structure is 2.6 kcal/mol lower than that of the AHM-b structure, which indicates that AHM-a is more stable. Thus, structure AHM-a is likely to exist.

Table 1
Geometrical information of chemical sensor AHM

	$\angle\text{C}_3\text{C}_2\text{N}_1\text{C}_4$	$\angle\text{C}_2\text{N}_1\text{C}_4\text{C}_5$	$\angle\text{O}_1\text{H}_1\text{N}_1$	O ₁ -H ₁	H ₁ -N ₁
AHM-a-S ₀	157°	177°	149°	1.01Å	1.64Å
AHM-b-S ₀	47°	179°	148°	1.01Å	1.63Å
AHM-c-S ₀	138°	177°	138°	1.70Å	1.03Å
AHM-d-S ₀	137°	-12°	129°	0.97 Å	2.40 Å
AHM-TICT	-179°	91°	144°	0.98Å	1.84Å
AHM-c-S ₁	173°	-179°	148°	1.58Å	1.05Å

[a] All the data are obtained at the B3LYP/TZVP theory level.

Excitation and emission process of AHM

In order to explore the photophysical properties of the sensor, the excitation and emission process of AHM were further analyzed. The calculated wavelengths and other data are listed in Table 2. As seen in Table 2, the S₀→S₁ transition for AHM-a is predicted at about 403 nm with oscillator strength of 0.7211, and the process is from HOMO to LUMO. For S₀→S₁ of AHM-a, during the excitation process, the distribution region of the electron does not change significantly, which also means that the excitation of S₀→S₁ is a local excitation (LE). Here, hole-electron analysis is also used. And only 0.08 electrons are transferred between the A part and B part. In addition, as listed in Table 3, the D index is relatively small, which provides direct evidence for proving that S₀→S₁ is LE state. The proton transfer reaction, triggered by a strong hydrogen bond between H₁ and N₁, could generate the new isomer AHM-c (Fig. 1c) was obtained by the ground state relaxation scanning the distance between H₁ and N₁. As shown in Table 1, $\angle\text{C}_3\text{C}_2\text{N}_1\text{C}_4$ and $\angle\text{C}_2\text{N}_1\text{C}_4\text{C}_5$ are 138° and 177°, respectively. As depicted in Fig. 1d, the product AHM-c is more stable than AHM-a. Also, the GS IPT energy barrier from AHM-a to AHM-c is merely 2.4 kcal/mol which indicates that the AHM-c structure is the most likely configuration. Consequently, the excitation and emission process of AHM-c will be further explored.

As is reported in Table 2, the dominant transition of AHM-c is the S₀→S₁ transition, with the oscillator strength of 0.5271 lying at 410 nm, which is assigned to HOMO→LUMO (98.1%) transition. The orbitals

are plotted in Fig. 2. A total of 0.16 electrons are transferred from the A part to the B part during the excitation, and the charge transfer is not obvious. Moreover, the D index is relatively small, which means that the $S_0 \rightarrow S_1$ of AHM-c is a LE state. The geometry in the S_1 state is optimized and given in Fig. 3a and Table 1. The $C_3C_2N_1C_4$ dihedral angle is 173° , which means there is a near planar structure in the S_1 state. The fluorescence quenching is not caused by planar structure. As listed in Table 2, AHM-c is a bright state in the S_1 state, and its oscillator strength is 0.9065. The calculated emission peak is 504 nm, which is consistent with the experimental value (500 nm). As is shown, the HOMO mainly distributes on the A part and B part while LUMO mainly distributes on the A part and C = N part. According to the hole-electron analysis, the charge transfer amount is relatively small (0.14 e). It is worth noting that the emission intensity observed at 500nm in the experiment is very weak, so the existence of a non-emission deactivation channel is assumed.

Table 2

Excitation and emission energies of the AHM, including the oscillator strength (f) and orbital transition (OT) contributions to the electronic excited states (CI).

	transition	λ (nm/eV)	f	OT	CI(%)
Experiment					
absorption		400/3.10			
emission		500/2.48			
AHM-a-S ₀	S ₀ →S ₁	403/3.07	0.7211	H→L	98.3%
	S ₀ →S ₂	327/3.78	0.0406	H-1→L	90.3%
	S ₀ →S ₃	315/3.92	0.0508	H-2→L	85.6%
				H→L + 2	5.4%
	S ₀ →S ₄	300/4.12	0.0315	H→L + 1	87.9%
AHM-b-S ₀	S ₀ →S ₁	403/3.07	0.5952	H→L	95.4%
	S ₀ →S ₂	339//3.65	0.0123	H-1→L	90.1%
	S ₀ →S ₃	317/3.91	0.0836	H-2→L	88.5%
				H→L + 3	7.3%
	S ₀ →S ₄	299/4.14	0.0178	H→L + 1	92.3%
AHM-c-S ₀	S ₀ →S ₁	410/3.02	0.5271	H→L	98.1%
	S ₀ →S ₂	349/3.55	0.0246	H-1→L	40.6%
	S ₀ →S ₃	336/3.68	0.1087	H-1→L	51.3%
	S ₀ →S ₄	308/4.02	0.0806	H-2→L	42.3%
AHM-c-S ₁	S ₁ →S ₀	504/2.45	0.9065	L→H	99.4%
AHM-TICT	S ₁ →S ₀	4016/0.30	0.0001	L→H	99.4%
AHM-a-S ₀ , AHM-b-S ₀ and AHM-c-S ₀ represent S ₀ state structures of a, b and c respectively. AHM-c-S ₁ represents S ₁ state structures of c. All the data are obtained at the B3LYP/TZVP theory level.					

Table 3

The exponent of the excited states for the sensor AHM, including the centroid distance (D), the degree of overlap (S_r), the width distribution (H), degree of separation (t), hole delocalization index (HDI) and electron delocalization index (EDI).

	D(Å)	S_r	H(Å)	t(Å)	HDI	EDI
AHM-a $S_0 \rightarrow S_1$	0.63	0.73	3.45	-0.86	6.31	7.42
AHM-a $S_0 \rightarrow S_3$	1.66	0.74	3.18	-2.32	6.66	7.22
AHM-b $S_0 \rightarrow S_1$	0.68	0.69	3.33	-1.58	6.66	7.94
AHM-c $S_0 \rightarrow S_1$	0.72	0.71	3.26	-1.77	7.06	7.93

The origination of the non-emissive behavior of AHM

Generally, bending of the C = N double bond may result in the formation of non-luminous isomers. As shown in Fig. 4, the bending degree of AHM-a in the S_0 state was studied by relaxing and scanning the dihedral angle of $C_2N_1C_4C_5$. The $\angle C_2N_1C_4$ of AHM-a- S_0 (Fig. 4a) and AHM-d- S_0 (Fig. 4c) structure are 124° and 122° , respectively. As shown in Fig. 5, the structure of AHM-a in the S_1 state was firstly optimized, and a distorted structure was found. The local HOMO is delocalized through the B part, and LUMO is mainly localized on the C = N and A part, with complete charge separation. Furthermore, a total of 0.40 electrons are transferred from the left moiety to the right moiety during the $S_1 \rightarrow S_0$ excitation by using hole-electron analysis. As listed in Table 1, $\angle C_3C_2N_1C_4$ and $\angle C_2N_1C_4C_5$ are -179° and 91° , respectively. Moreover, by TDDFT calculation, the oscillator strength is almost zero (0.0001). This indicates that in the S_1 state, AHM-a is a typical TICT state and then named as AHM-TICT. However, the bending angle of the N_1-C_4 double bond requires the energy of 30.17 kcal/mol. Thus, the TICT state cannot be attained by direct excitation and excited state relaxation from AHM-d- S_0 .

In order to explore the pathway to the TICT state, the H_1-N_1 distance of AHM-c in the S_1 state was relaxed-scanned. As shown in Fig. 6, the energy barrier of ESIPT from AHM-c- S_1 to the transition state is merely 2.08 kcal/mol. Moreover, the product produced by ESIPT happens to be AHM-a- S_1 , also known as AHM-TICT, which indicates that ESIPT triggers the distortion of the structure and spontaneously reaches the TICT state. Due to the higher energy barrier from AHM-a to AHM-d, it is difficult to form AHM-d structure. In the S_1 state, AHM-c carries out ESIPT process and further triggers the TICT state.

IR vibrational spectra and RDG isosurfaces of sensor AHM

See in Fig. S1, the IR spectra of the main hydrogen bonds involved in the S_0 and S_1 states have been computed. For the AHM, the O_1-H_1 peak shifts from 3563 cm^{-1} in the S_0 state to 2945 cm^{-1} in the S_1

state. The IR vibrational frequency of O₁-H₁ bond of AHM has a red shift of 618 cm⁻¹, which indicates that the AHM sensor has a large Stokes shift. It can also be manifested that the intramolecular hydrogen bond in S₁ state is much stronger than that in S₀ state through the analysis of stretching vibration frequencies.

As shown in the RDG scatter graph of Fig. S2 (a), the value range of the RDG isosurfaces is set from -0.05 to 0.05. The spike peaks of the AHM complex are observed and located at -0.0408 (Fig. S2 (b)). The interaction type is assigned to hydrogen bond interaction and the more to the left of the peak, the stronger the hydrogen bond is. In the diagram, it can be seen that the part representing the hydrogen bonding interaction in O₁-H₁...N₁ presents a ring in the RDG isosurfaces. There is a strong hydrogen bond interaction between H proton and N receptor in the S₁ state.

Al³⁺ sensing mechanism of AHM

In the previous sections, the photo-physical process of the AHM was clarified. Next, the Al³⁺ detecting mechanism is explored. The reaction sites of hydrogen bonded donor and acceptor and their interactions can be analyzed by electrostatic potential (ESP). As shown in Fig. 7a, the ESP surface of AHM in the S₀ state is studied. The yellow ball and the blue ball correspond to the maximum and minimum values of the electrostatic potential respectively. The most negative site is located near O₁ atom, and its value is -125kJ/mol. Thus, the interaction between Al³⁺ and the O₁ position should be strong. Then, the complex formed between AHM and Al³⁺, is optimized, shown in Fig. 7b. Detailed geometric parameters are listed in Table 4. In order to ensure the rationality of the configuration in the coordination regions, Mayer bond order analyses of the AHM-Al is conducted through the Multiwfn program. The Mayer bond orders of three bonds (Al-O₁, Al-O₂, Al-N₁) are 0.73, 0.72, 0.53 respectively. These results indicate that the bonds of the Al-O₁, Al-O₂ and Al-N₁ are the coordinate bond. And the coordinate bond of Al-O₁ and Al-O₂ are stronger than Al-N₁ coordinate bond in the AHM-Al complexes.

As listed in Table 4, the structure of AHM-Al in the S₁ state is very similar to that in the S₀ state. In the S₁ state, the flatness of the molecule increases and the non-emitting TICT state is eliminated. Furthermore, the HOMO and LUMO orbitals of the ligand (AHM-a) and the complexes (AHM-Al) are also compared and analyzed. The energy gaps between HOMO and LUMO are found as 3.526 eV and 2.479 eV, respectively, for AHM-a and AHM-Al complex (Fig. 8). This indicates that AHM-Al complex is more stabilized than that of AHM-a. For AHM-Al, the electron is confined to the A part, and the distribution region of the electron does not change significantly before and after the excitation. Meanwhile, the emission process of AHM-Al is studied. As shown in Table 5, the S₁→S₀ emission with large oscillator strength of 0.9313 generates π→π* transition character, which means the AHM-Al is emissive. Moreover, Al³⁺ is not involved in the emission process, who eliminates the original TICT state.

Table 4

eometries of the complex (at B3LYP/TZVP theory level).

	AHM-Al-S ₀	AHM-Al-S ₁
$\angle C_3C_2N_1C_4$	149°	153°
$\angle C_2N_1C_4C_5$	-161°	-169°
$\angle N_1C_4C_5C_6$	19°	16°
Al-O ₁	1.79Å(0.73)	1.72Å(0.74)
Al-O ₂	1.84Å(0.72)	1.77Å(0.71)
Al-N ₁	1.95Å(0.53)	1.85Å(0.55)
[a] The values in the brackets are calculated Mayer bond orders. [42]		

Table 5

Excitation and emission energies of the metal-sensor complexes (B3LYP/ TZVP).

	transition	λ (nm/eV)	<i>f</i>	OT	CI (%)
AHM-Al-S ₀	S ₀ →S ₁	431/2.87	1.2638	H→L	94.4%
	S ₀ →S ₂	422/2.94	0.0214	H→L	50%
				H-1→L	38%
	S ₀ →S ₃	411/3.01	0.1623	H-1→L	92%
AHM-Al-S ₁	S ₁ →S ₀	530/2.34	0.9313	L→H	97%
^a AHM-Al represents the triple-coordinated organometallic compound formed between AHM and Al ³⁺ .					

Conclusions

In conclusion, the sensor AHM has been researched and analyzed by DFT and TDDFT theoretical methods. The imine nitrogen of the sensor is adjacent to the -OH group, and the sensor has a large spectral shift for Al³⁺ ions due to the presence of polar groups such as hydroxyl and amine. Furthermore, the trivalent form of these groups has a high affinity for the Al³⁺ ion. In acetonitrile solvent, the AHM exhibits weak fluorescence emission because of ES IPT and C = N isomerization. Upon adding of Al³⁺, the AHM coordinates with the metal ions and eliminates the TICT state. The coordination Al³⁺ with AHM deprotonates the phenolic hydroxyl groups preventing the intrahydrogen bonding with imine nitrogen (O-

H⁺N) and also inhibits the ES IPT. Based on the characteristics of sensor AHM, it is widely used in real life, such as cell imaging and dipstrip test.

Declarations

Funding This work was supported by the Open Project of SKLMRD (the open fund of the state key laboratory of molecular reaction dynamics in DICP, CAS) and the General Program from Education department of Liaoning Province (Grant LJKZ0534).

Conflicts of interest The authors declare no competing interest.

Availability of data and material Not applicable

Code availability Not applicable

Authors' contributions The data collection, analysis, writing were performed by Xiumin Liu. The data collection, analysis were performed by Hengwei Zhang. The data analysis was performed by Sen Liu. The study's conception, design, data collection, analysis, writing, editing, review, and supervision were performed by Yi Wang. The study's conception, editing, review, and supervision were performed by Peng Zhang.

References

1. He ZL, Yang XE, Stoffella PJ (2005) Trace elements in agroecosystems and impact on the environment. *J Trace Elem Med Biol* 19:125–140. <https://doi.org/10.1016/j.jtemb.2005.02.010>
2. Aron AT, Ramos-Torres KM, Cotruvo Jr JA et al (2015) Recognition-and reactivity-based fluorescent probes for studying transition metal signaling in living systems. *Acc Chem Res* 48:2434–2442. <https://doi.org/10.1021/acs.accounts.5b00221>
3. Sorenson JR, Campbell IR, Tepper LB et al (1974) Aluminum in the environment and human health. *Environ Health Perspect* 8:3–95. <https://doi.org/10.1289/ehp.7483>
4. Litov RE, Sickles VS, Chan GM et al (1989) Plasma aluminum measurements in term infants fed human milk or a soy-based infant formula. *Pediatrics* 84:1105–1107.
5. Yokel RA, Hicks CL, Florence RL (2008) Aluminum bioavailability from basic sodium aluminum phosphate, an approved food additive emulsifying agent, incorporated in cheese. *Food Chem Toxicol* 46:2261–2266. <https://doi.org/10.1016/j.fct.2008.03.004>
6. Soni MG, White SM, Flamm WG et al (2001) Safety evaluation of dietary aluminum. *Regul Toxicol Pharm* 33:66–79. <https://doi.org/10.1006/rtph.2000.1441>
7. Doherty RE (2000) A history of the production and use of carbon tetrachloride, tetrachloroethylene, trichloroethylene and 1, 1, 1-trichloroethane in the United States: part 2—trichloroethylene and 1, 1, 1-trichloroethane. *Environ Forensics* 1:83–93. <https://doi.org/10.1006/enfo.2000.0011>

8. House E, Esiri M, Forster G et al (2012) Aluminium, iron and copper in human brain tissues donated to the medical research council's cognitive function and ageing study. *Metallomics*4:56–65. <https://doi.org/10.1039/c1mt00139f>
9. Mirza A, King A, Troakes C et al (2017) Aluminium in brain tissue in familial Alzheimer's disease. *Journal of trace elements in medicine and biology: organ of the Society for Minerals and Trace Elements*. 40:30–36. <https://doi.org/10.1016/j.jtemb.2016.12.001>
10. Nayak P (2002) Aluminum: impacts and disease. *Environ Res*89:101–115. <https://doi.org/10.1006/enrs.2002.4352>
11. Good PF, Olanow C, Perl DP (1992) Neuromelanin-containing neurons of the substantia nigra accumulate iron and aluminum in Parkinson's disease: a LAMMA study. *Brain Res*593:343–346. [https://doi.org/10.1016/0006-8993\(92\)91334-b](https://doi.org/10.1016/0006-8993(92)91334-b)
12. Yumoto S, Kakimi S, Ishikawa A (2009) Demonstration of aluminum in amyloid fibers in the cores of senile plaques in the brains of patients with Alzheimer's disease. *J Inorg Biochem* 103:1579–1584. <https://doi.org/10.1016/j.jinorgbio.2009.07.023>
13. Rondeau V, Jacqmin-Gadda H, Commenges D et al (2009) Aluminum and silica in drinking water and the risk of Alzheimer's disease or cognitive decline: findings from 15-year follow-up of the PAQUID cohort. *Am J Epidemiol* 169:489–496. <https://doi.org/10.1093/aje/kwn348>
14. Sahana A, Banerjee A, Das S et al (2011) A naphthalene-based Al³⁺ selective fluorescent sensor for living cell imaging. *Org Biomol Chem*9:5523–5529. <https://doi.org/10.1039/c1ob05479a>
15. Zhao Q, Li F, Huang C (2010) Phosphorescent chemosensors based on heavy-metal complexes. *Chem Soc Rev*39:3007–3030. <https://doi.org/10.1039/b915340c>
16. Zhang JF, Zhou Y, Yoon J et al (2011) Recent progress in fluorescent and colorimetric chemosensors for detection of precious metal ions (silver, gold and platinum ions). *Chem Soc Rev*40:3416–3429. <https://doi.org/10.1039/c1cs15028f>
17. Kaur K, Saini R, Kumar A et al (2012) Chemodosimeters: an approach for detection and estimation of biologically and medically relevant metal ions, anions and thiols. *Coord Chem Rev*256:1992–2028.
18. Yang Y, Zhao Q, Feng W et al (2013) Luminescent chemodosimeters for bioimaging. *Chem Rev*113:192–270. <https://doi.org/10.1021/cr2004103>
19. Schneider HJ, Yatsimirsky AK (2000) Principles and Methods in Supramolecular Chemistry. J Wiley <https://doi.org/10.1002/9783527644131>
20. Zhang M, Yu MX, Li FY et al (2007) A Highly Selective Fluorescence Turn-on Sensor for Cysteine/Homocysteine and Its Application in Bioimaging. *J Am Chem. Soc*129:10322–10323. <https://doi.org/10.1021/ja073140i>
21. Zhao M, Ma L, Zhang M et al (2013) Glutamine-containing “turn-on” fluorescence sensor for the highly sensitive and selective detection of chromium (III) ion in water. *J Spectrochim Acta Part A* 116:460–465. <https://doi.org/10.1016/j.saa.2013.07.069>

22. Wu JS, Liu MW, Zhuang XQ (2007) Fluorescence Turn On of Coumarin Derivatives by Metal Cations: A New Signaling Mechanism Based on C=N Isomerization. *Org Lett* 9:33–36. <https://doi.org/10.1021/ol062518z>
23. Tang XL, Peng XH, Dou W et al (2008) Design of a Semirigid Molecule as a Selective Fluorescent Chemosensor for Recognition of Cd(II). *Org Lett* 10:3653–3656. <https://doi.org/10.1021/ol801382f>
24. Li L, Dang YQ, Li HW et al (2010) Integrated genomic analyses of ovarian carcinoma. *Tetrahedron Lett* 51:618–621. <https://doi.org/10.1038/nature10166>
25. Liu YJ, Tian FF, Fan XY et al (2017) Fabrication of an acylhydrazone based fluorescence probe for Al³⁺. *Sensors Actuators B Chem* 240:916–925. <https://doi.org/10.1016/j.snb.2016.09.051>
26. Upadhyay Y, Bothra S, Kumar, R.; Choi, H. J.; Sahoo, S K. Optical sensing of hydrogen sulphate using rhodamine 6G hydrazide from aqueous medium. *Spectrochim Acta A* 180:44–50. <https://doi.org/10.1016/j.saa.2017.02.057>
27. Fang TC, Tsai HY, Luo MH et al (2013) Excited-state chargecoupled proton transfer reaction via the dipolar functionality of Salicylideneaniline. *Chin Chem Lett* 24:145–148. <https://doi.org/10.1016/j.ccllet.2013.01.011>
28. Jana S, Dalapati S, Guchhait N (2012) Proton transfer assisted charge transfer phenomena in photochromic schiff bases and effect of –NEt₂ groups to the AnilSchiff bases. *J Phys Chem A* 116:10948–10958. <https://doi.org/10.1021/jp3079698>
29. Li W, Tian X, Huang B et al (2016) Triphenylamine-based Schiff bases as the High sensitive Al³⁺ or Zn²⁺ fluorescence turn-on probe: mechanism and application in vitro and in vivo. *Biosens Bioelectron* 77:530–536. <https://doi.org/10.1016/j.bios.2015.09.059>
30. Rodríguez-Córdoba W, Zugazagoitia JS, Collado-Fregoso E et al (2007) Excited state intramolecular proton transfer in schiff bases. Decay of the locally excited enol state observed by femtosecond resolved fluorescence. *J Phys Chem A* 111:6241–6247. <https://doi.org/10.1021/jp072415d>
31. Yu FS, Guo XF, Tian XJ et al (2017) A Ratiometric Fluorescent Sensor for Zn²⁺ Based on N,N'-Di(quinolin-8-yl)oxalamide. *J Fluoresc* 27:723–728. <https://doi.org/10.1007/s10895-016-2003-0>
32. Mummidivarapu VVS, Tabbasum K, China JP et al (2012) 1,3-di-amidoquinoline conjugate of calix[4]arene(L) as a ratiometric and colorimetric sensor for Zn²⁺: spectroscopy, microscopy and computational studies. *Dalton Trans.* 41:1671–1674. <https://doi.org/10.1039/c2dt11900e>
33. Stasiuk GJ, Minuzzi F, Sae-Heng M et al (2015) Dual-modal magnetic resonance/fluorescent zinc sensors for pancreatic β-cell mass imaging. *Chem Eur J* 21:5023–5033. <https://doi.org/10.1002/chem.201406008>
34. Neetu Yadav, Ashok Kumar Singh (2018) A turn-on ESIPT based fluorescent sensor for detection of aluminum ion with bacterial cell imaging and logic gate applications. *Materials Science & Engineering C* 90:468-475. <https://doi.org/10.1016/j.msec.2018.04.087>
35. Frisch MJ, Trucks GW, Schlegel HB et al (2016) Gaussian, Inc., Wallingford CT.

36. Becke AD (1988) Density-functional exchange-energy approximation with correct asymptotic behavior. *Phys Rev A* 38:3098–3100.
37. Schafer A, Horn H, Ahlrichs R (1992) Fully optimized contracted Gaussian basis sets for atoms Li to Kr. *J Chem Phys* 97:2571–2577. <https://doi.org/10.1063/1.463096>
38. Schafer A, Huber C, Ahlrichs R (1997) Fully optimized contracted Gaussian basis sets of triple zeta valence quality for atoms Li to Kr. *J Chem Phys* 100:5829–5835. <https://doi.org/10.1063/1.467146>
39. Cancès E, Mennucci B, Tomasi J (1997) A new integral equation formalism for the polarizable continuum model: theoretical background and applications to isotropic and anisotropic dielectrics. *J Chem Phys* 107:3032–3041. <https://doi.org/10.1063/1.474659>
40. Lu T, Chen FW (2012) Multiwfn: A multifunctional wavefunction analyzer. *J Comput Chem* 33:580–592. [10.1002/jcc.22885](https://doi.org/10.1002/jcc.22885)
41. Johnson ER, Keinan S, Sanchez PM et al (2010) Revealing noncovalent interactions. *J Am Chem Soc* 132:6498–6506. <https://doi.org/10.1021/ja100936w>
42. Mayer I (1983) Charge, bond order and valence in the AB initio SCF theory. *Chem Phys Lett* 97:270–274.

Figures

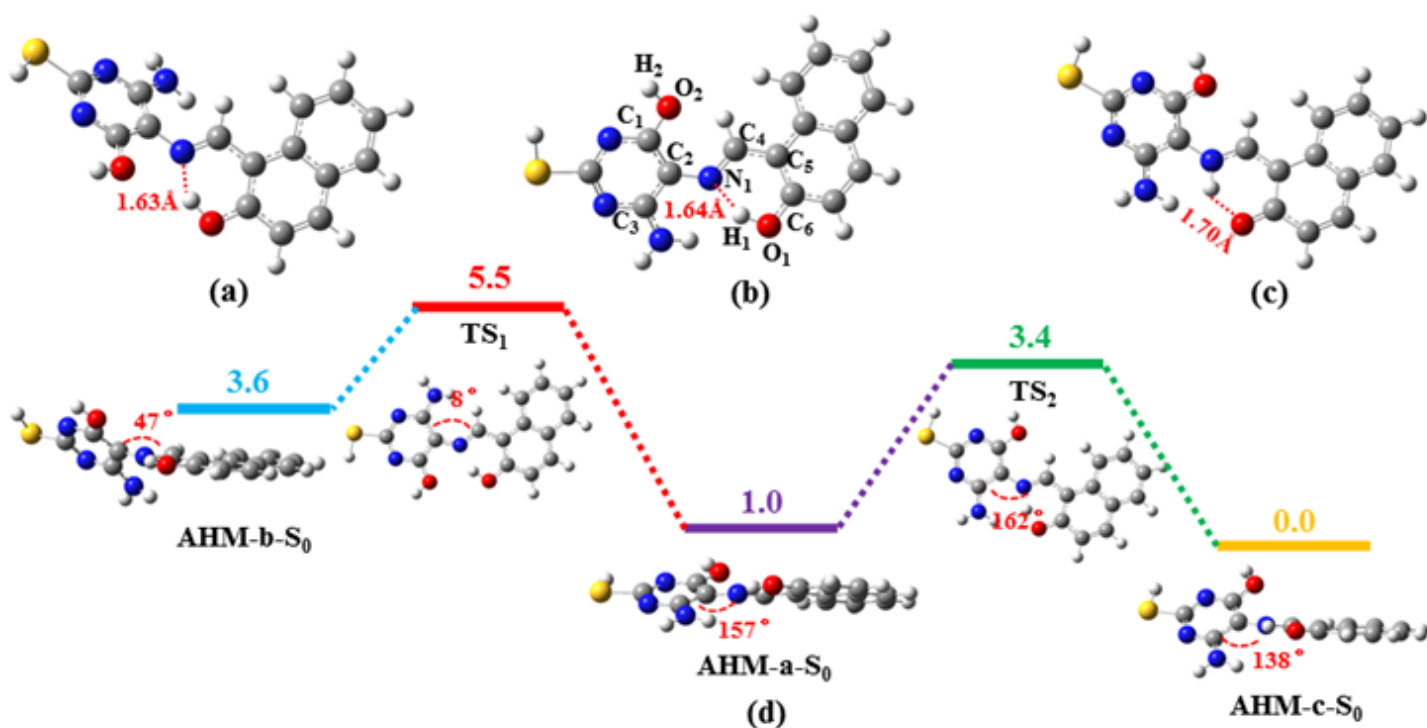


Figure 1

(a) Optimized structure of AHM-b in the ground state (AHM-b-S₀); (b) optimized structure of AHM-a in the ground state (AHM-a-S₀); (c) optimized structure of AHM-c in the ground state (AHM-c-S₀); (d) Energy barriers for the torsion of the C₃C₂N₁C₄ dihedral and the GSIPT process in the ground state (energies are given in kcal/mol; lengths are given in Angstrom).

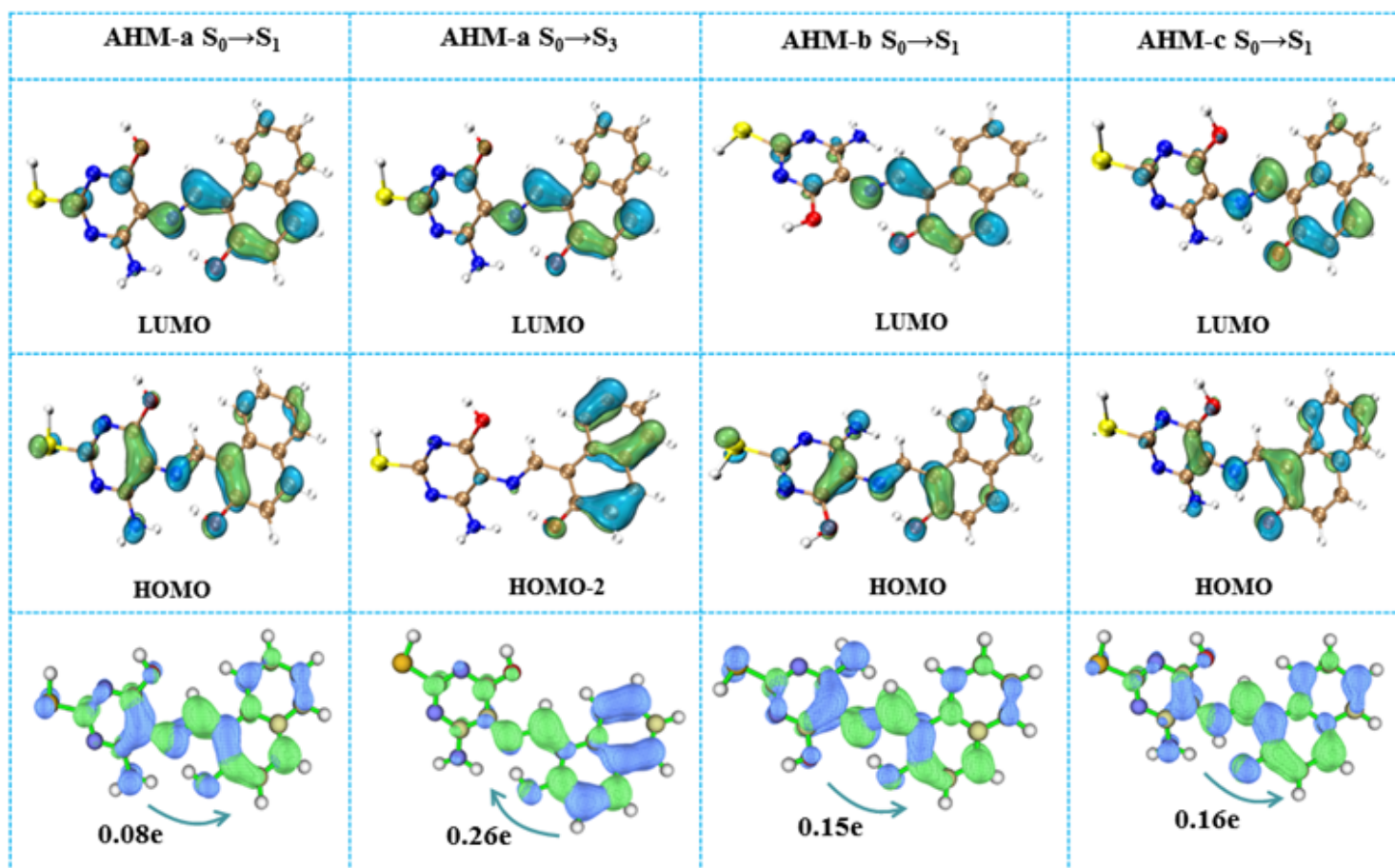


Figure 2

Molecular orbitals involved in the excitation processes of the sensor AHM (the blue iso-surface represents the hole distribution and the green iso-surface represents the electron distribution).

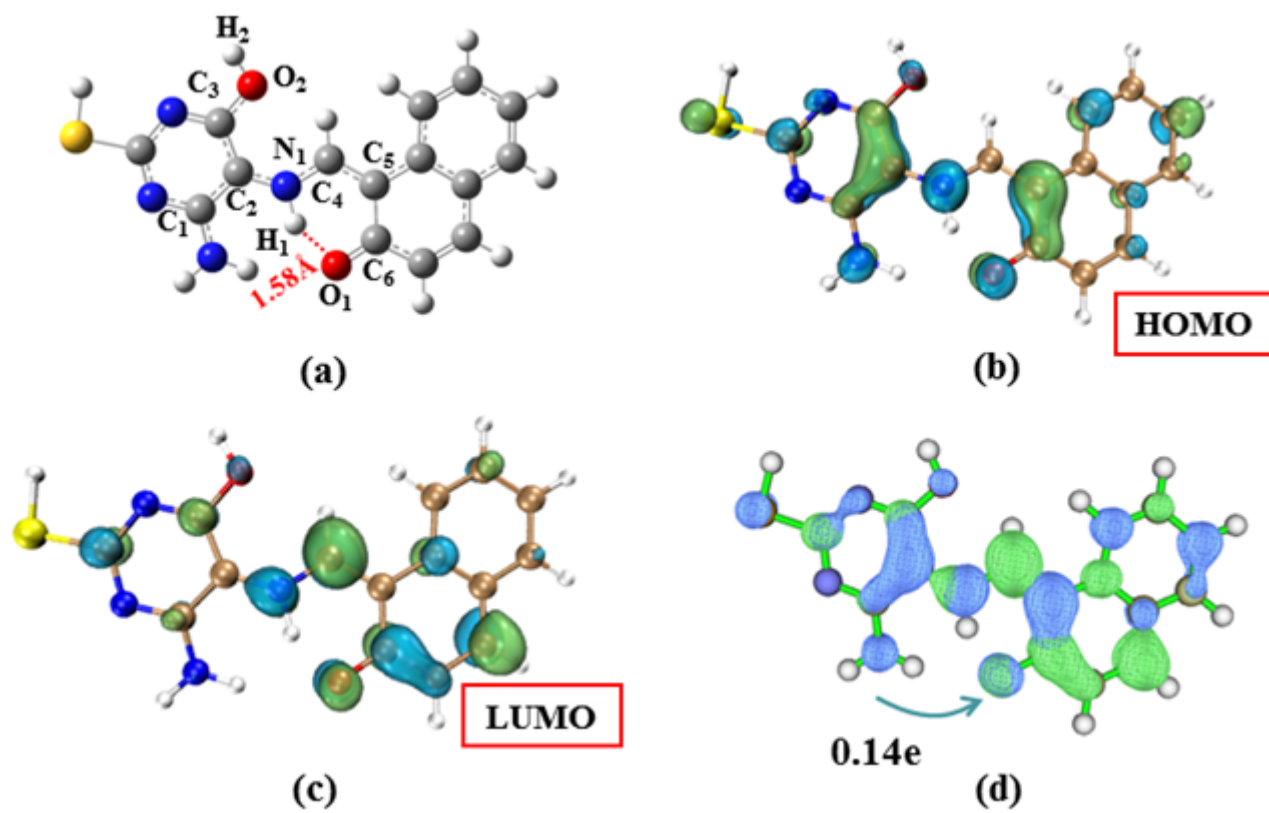


Figure 3

(a) Optimized structure of AHM-c (AHM-c- S_1) in the S_1 state; (b) HOMO of AHM-c- S_1 ; (c) LUMO of AHM-c- S_1 ; (d) The electron-hole distribution of AHM-c- S_1 .

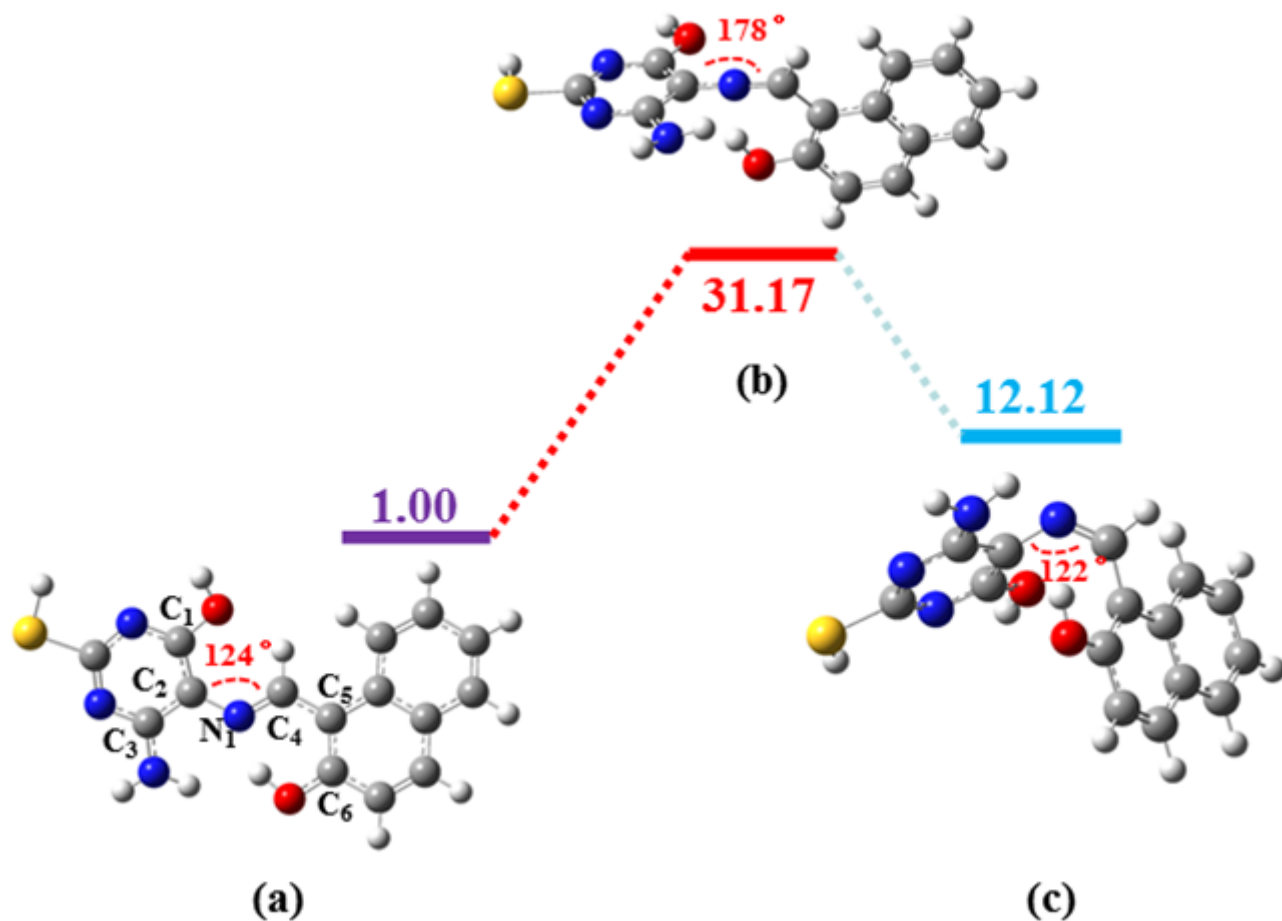


Figure 4

(a) The structure of AHM-a in the S_0 state; (b) Energy barrier and transition state for the bending of N_1-C_4 double bond in the S_0 state (energies are given in kcal/mol); (c) The structure of the bending product in the S_0 state (AHM-d- S_0).

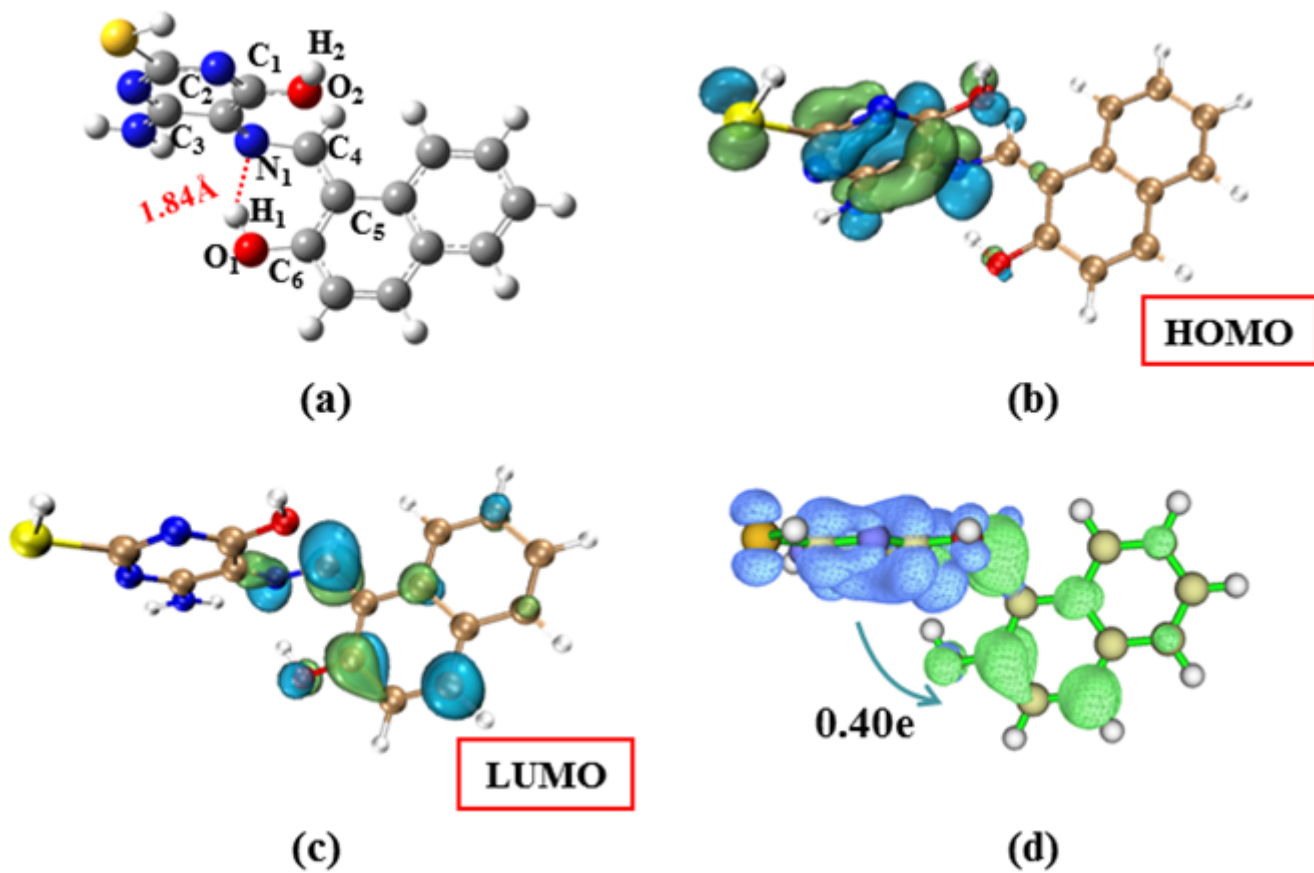


Figure 5

(a) Optimized structure of AHM-a (AHM-a-S₁) in the S₁ state; (b) HOMO of AHM-a-S₁; (c) LUMO of AHM-a-S₁; (d) electron-hole distribution of the excited state deactivation process.

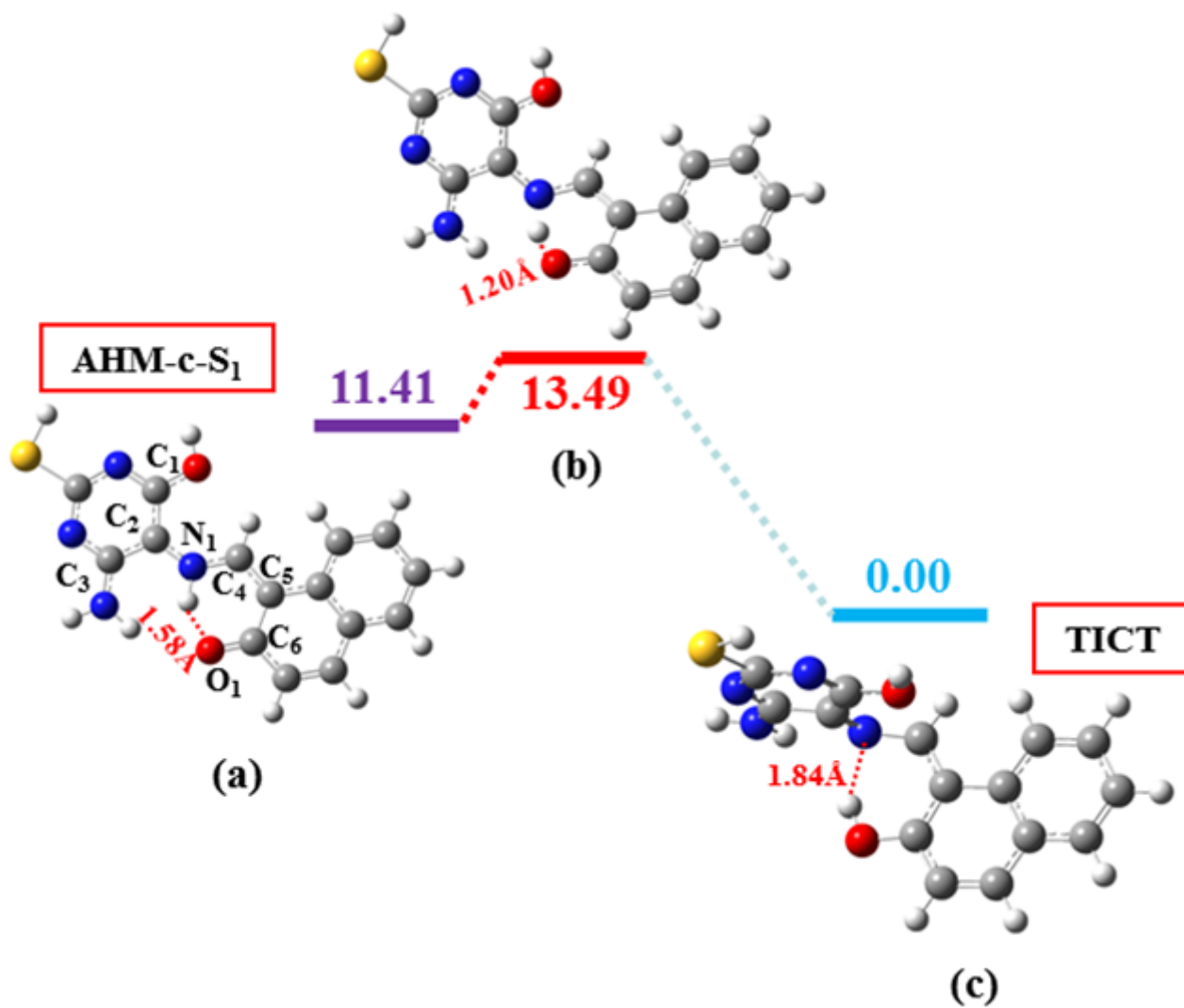
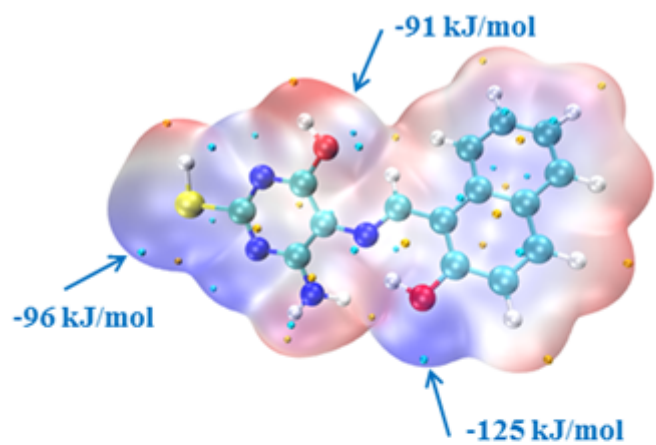
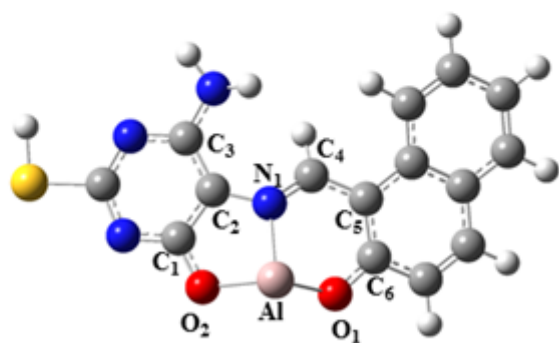


Figure 6

(a) The structure of AHM-c in the S_1 state; (b) Energy barrier and transition state for ESIPT of AHM-c in the S_1 state (energies are given in kcal/mol); (c) The structure of AHM-TICT.



(a)



(b)

Figure 7

(a) Electrostatic potential (ESP) surface of the sensor in the S_0 state (blue surface represents negative regions on the ESP surface); (b) geometry of the AHM-Al complex in the S_0 state

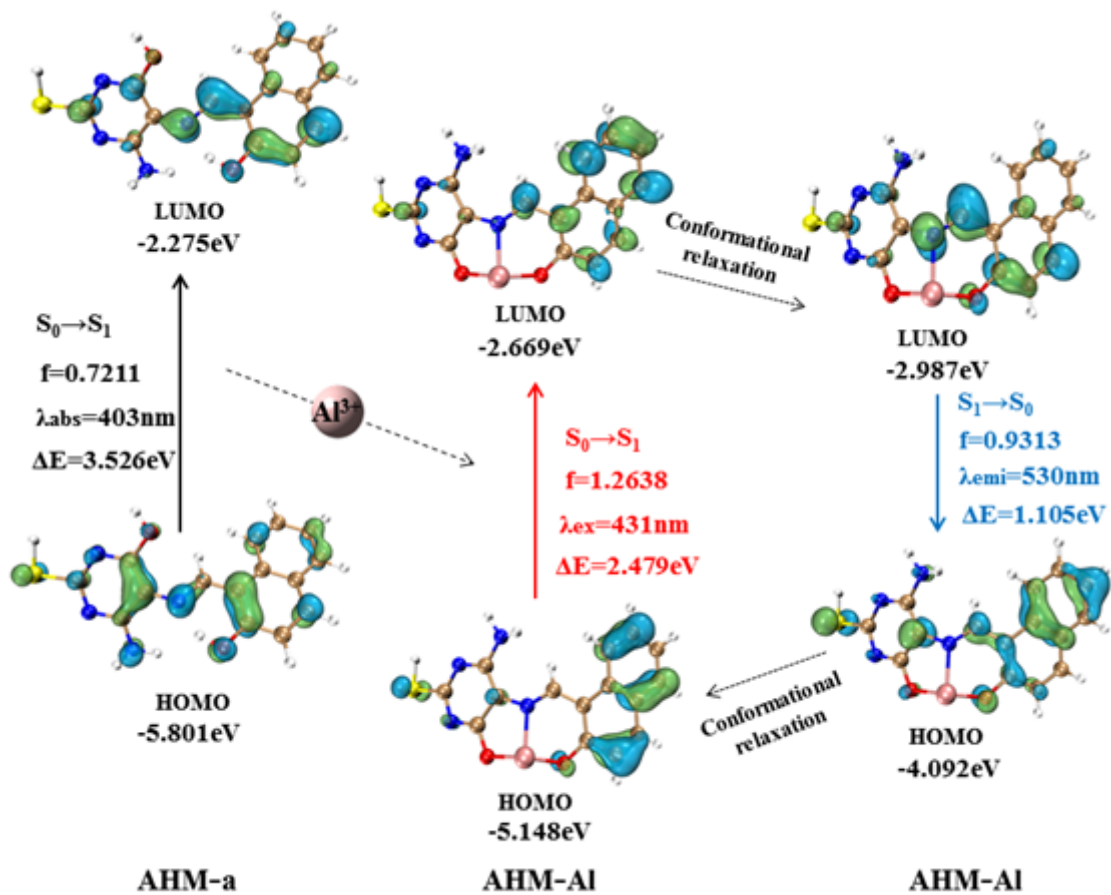


Figure 8

Frontier molecular orbitals involved in the UV-vis absorption of AHM and AHM-Al complex and the emission of AHM-Al.